


Article

# Synthesis Method and Thermodynamic Characteristics of Anode Material $\text{Li}_3\text{FeN}_2$ for Application in Lithium-Ion Batteries

Anatoliy Popovich <sup>1</sup>, Pavel Novikov <sup>1</sup>, Qingsheng Wang <sup>2</sup>, Konstantin Pushnitsa <sup>1</sup> and Daniil Aleksandrov <sup>1,\*</sup> 

<sup>1</sup> Institute of Machinery, Materials, and Transport, Peter the Great St. Petersburg Polytechnic University, 195251 Saint Petersburg, Russia; director@immet.spbstu.ru (A.P.); novikov\_pa@spbstu.ru (P.N.); pushnitsa\_ka@spbstu.ru (K.P.)

<sup>2</sup> CHN/RUS New Energy and Material Technology Research Institute, Huzhou 313100, China; envbattery@yandex.ru

\* Correspondence: aleksandrov\_ds@spbstu.ru

**Abstract:**  $\text{Li}_3\text{FeN}_2$  material was synthesized by the two-step solid-state method from  $\text{Li}_3\text{N}$  (adiabatic camera) and  $\text{FeN}_2$  (tube furnace) powders. Phase investigation of  $\text{Li}_3\text{N}$ ,  $\text{FeN}_2$ , and  $\text{Li}_3\text{FeN}_2$  was carried out. The discharge capacity of  $\text{Li}_3\text{FeN}_2$  is  $343 \text{ mAh g}^{-1}$ , which is about 44.7% of the theoretic capacity. The ternary nitride  $\text{Li}_3\text{FeN}_2$  molar heat capacity is calculated using the formula  $C_{p,m} = 77.831 + 0.130 \times T - 6289 \times T^{-2}$ , ( $T$  is absolute temperature, temperature range is 298–900 K, pressure is constant). The thermodynamic characteristics of  $\text{Li}_3\text{FeN}_2$  have the following values: entropy  $S^0_{298} = 116.2 \text{ J mol}^{-1} \text{ K}^{-1}$ , molar enthalpy of dissolution  $\Delta_d H_{\text{LFN}} = -206.537 \pm 2.8 \text{ kJ mol}^{-1}$ , the standard enthalpy of formation  $\Delta_f H^0 = -291.331 \pm 5.7 \text{ kJ mol}^{-1}$ , entropy  $S^0_{298} = 113.2 \text{ J mol}^{-1} \text{ K}^{-1}$  (Neumann–Kopp rule) and  $116.2 \text{ J mol}^{-1} \text{ K}^{-1}$  (W. Herz rule), the standard Gibbs free energy of formation  $\Delta_f G^0_{298} = -276.7 \text{ kJ mol}^{-1}$ .



**Citation:** Popovich, A.; Novikov, P.; Wang, Q.; Pushnitsa, K.; Aleksandrov, D. Synthesis Method and Thermodynamic Characteristics of Anode Material  $\text{Li}_3\text{FeN}_2$  for Application in Lithium-Ion Batteries. *Materials* **2021**, *14*, 7562. <https://doi.org/10.3390/ma14247562>

Received: 1 October 2021

Accepted: 2 December 2021

Published: 9 December 2021

**Publisher's Note:** MDPI stays neutral with regard to jurisdictional claims in published maps and institutional affiliations.



**Copyright:** © 2021 by the authors. Licensee MDPI, Basel, Switzerland. This article is an open access article distributed under the terms and conditions of the Creative Commons Attribution (CC BY) license (<https://creativecommons.org/licenses/by/4.0/>).

**Keywords:** lithium-ion battery; anode battery; lithium-ion thermodynamics; solid-state synthesis

## 1. Introduction

In the world of technological development, energy sources are being severely depleted. In this regard, the issues related to creating new energy sources, in particular renewable energy sources, are being considered.

Secondary batteries, such as lithium-ion, lithium sulfur, and hydrogen batteries, are attracting increased attention for their development and production. Probably, one of the prospective renewable sources of energy is the lithium-ion battery (LIB) as an energy source for many applications, such as electric cars and buses, laptops, mobile phones, etc. LIBs solve the problems of high energy requirements (energy and power density, cycle life), environmental efforts, and relatively low cost.

A lot of efforts were directed to the development of more advanced batteries. For example, different approaches for LIB's development were used, such as nanostructured materials [1–13], the growth of the capacity and voltage of cathode materials [14–30], hollow and porous and structures [13,31–44], safety issues, including separator and liquid electrolyte studies [45–56], etc. As a prospective current source for electric vehicles (EV), LIBs have proven their market position. To receive high-performance lithium-ion batteries, it is required to improve the specific capacity of active (electrode) materials.

Thus, a lot of efforts were focused on the fabrication of anode materials with high theoretical specific capacity. For example, silicon has attracted the attention of the LIBs industry as an anode material with ultrahigh specific capacity ( $4212 \text{ mAhg}^{-1}$ ), although the large volume expansion of silicon during the charge/discharge process (300%) leads to a capacity decrease and reduced cycle life [57].

Another popular anode material with high performance is  $\text{Li}_4\text{Ti}_5\text{O}_{12}$ . This anode material attracted attention due to its low manufacturing cost, high safety, and environmental friendliness [58,59]. However,  $\text{Li}_4\text{Ti}_5\text{O}_{12}$  has poor electrical conductivity of  $10^{-8}$ – $10^{-13}$   $\text{S cm}^{-1}$ , a low lithium diffusion coefficient ( $10^{-9}$ – $10^{-16}$   $\text{cm}^2 \text{s}^{-1}$ ), and a low theoretical capacity of  $175 \text{ mAh g}^{-1}$  [60–63].

Previous works shows good electrochemical properties of  $\text{Li}_3\text{N}$ -type anodes, e.g.,  $\text{Li}_2\text{Na}_4\text{N}_2$  and  $\text{Li}_4\text{Na}_2\text{N}_2$  phases [64],  $\text{LiBeN}$  [65],  $\text{Li}_3\text{N-Mg}_3\text{N}_2$  [66],  $\text{Li}_{2n-1}\text{MN}$  [67], and  $\text{Li}_3\text{FeN}_2$  [68,69]. Thus, as  $\text{Li}_3\text{FeN}_2$  materials have transition metal, it could not be used as solid electrolyte because transition metals might produce conduction electrons, which is unacceptable for a solid electrolyte of lithium battery. However, this quality is advantageous for using this material as an electrode.  $\text{Li}_{3-x}\text{FeN}_2$  ( $0 < x < 1$ ) has a high capacity of  $260 \text{ mAh g}^{-1}$  [67]. In addition, the charge–discharge potentials between 0 and 2 V (vs. Li) were very flat for  $x = 0.1$ – $0.7$ .

$\text{Li}_3\text{FeN}_2$  was first synthesized by Frankenburger et al. by the reaction of lithium nitride ( $\text{Li}_3\text{N}$ ) with elemental Fe in  $\text{N}_2$  atmosphere [70]. After decades, Fromont investigated the reaction of  $\text{Li}_3\text{N}$  with iron using thermogravimetry [71]. These studies show that  $\text{Li}_3\text{FeN}_2$  was indexed by an orthorhombic cell with lattice parameters  $a = 9.65 \text{ \AA}$ ,  $b = 8.66 \text{ \AA}$ , and  $c = 8.38 \text{ \AA}$ . Emery et al. [70] show the solid-state synthesis of  $\text{Li}_3\text{N}$  with Fe powder in atmosphere, which shows a cationic mixing in  $\text{Li}_3\text{FeN}_2$  compound.

$\text{Li}_3\text{FeN}_2$  is a prospective material for hydrogen storage because of its hydrogen uptake capacity of 2.7 wt %, of which about 1.5 wt % was reversible [69,72,73].

In this article, the two-step synthesis and properties of promising anode material  $\text{Li}_3\text{FeN}_2$  are shown. Firstly,  $\text{Li}_3\text{N}$  synthesis was obtained in an adiabatic chamber. Then, mixed with iron nanopowder,  $\text{Li}_3\text{FeN}_2$  was obtained at a tube furnace. Two-step synthesis was chosen for the synthesis of high-purity complex nitride  $\text{Li}_3\text{FeN}_2$ .

## 2. Materials and Methods

A 16 mm diameter and 0.6 mm lithium plate sliced and polished in an argon glovebox, iron nanopowder, nitrogen, and ammonia ( $\text{NH}_3$ ) were used as starting components for  $\text{Li}_3\text{N}$ ,  $\text{Fe}_2\text{N}$ , and  $\text{Li}_3\text{FeN}_2$  synthesis (Table 1). The purity of materials shown in Table 1 is according to suppliers' data. Lithium sliced plates were put into a titanic autoclave nitrogen-filled bomb of Netzsch APTAC 264 (Selb, Germany), as shown in Figure 1. The  $\text{Li}_3\text{N}$  synthesis parameters are next: the temperature is  $170 \text{ }^\circ\text{C}$ , heat rate is  $2 \text{ }^\circ\text{C}/\text{min}$ , synthesis time is 6 h, and nitrogen pressure is  $\approx 709.3 \text{ kPa}$  (7 atm).

**Table 1.** Summary of chemicals descriptions.

Name	Formula	Source	Purity, %
Iron nanopowder	Fe	Changsha Easchem Co., Ltd. (Changsha, China)	99.9
Lithium	Li	Xiamen Tmax Battery Equipments Ltd. (Xiamen, China)	99.9
Nitrogen	$\text{N}_2$	Qingdao Guida Special Gas Co., Ltd. (Qingdao, China)	99.9–99.999
Ammonia	$\text{NH}_3$	Wuhan Newradar Trade Company Ltd. (Wuhan, China)	99.9
Lithium nitride	$\text{Li}_3\text{N}$	Prepared here	98.9 <sup>1</sup>
Iron nitride	$\text{Fe}_2\text{N}$	Prepared here	98.4 <sup>1</sup>
Lithium iron nitride	$\text{Li}_3\text{FeN}_2$	Prepared here	99.1 <sup>1</sup>

<sup>1</sup> Purity according to XRD analysis.

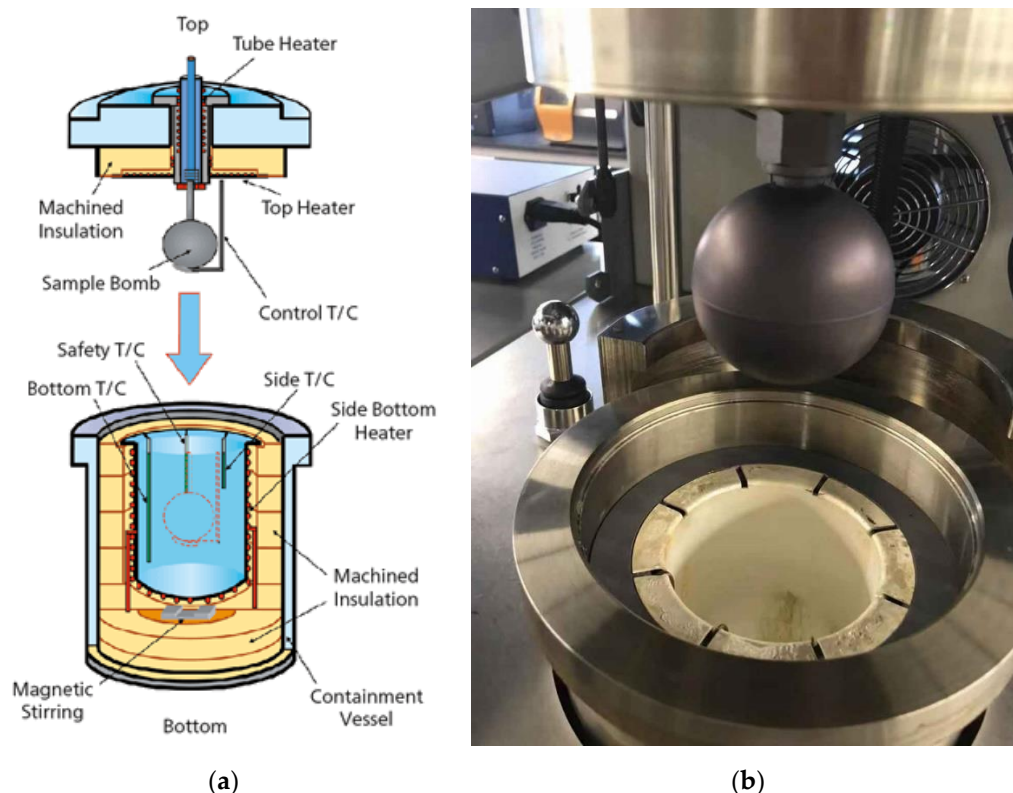


**Figure 1.** Scheme (a) and photo (b) of Netzsch APTAC chamber. 1—machined insulation; 2—sample bomb; 3—safety thermocouple; 4—bottom thermocouple; 5—magnetic stirring; 6—containment vessel; 7—machined insulation; 8—side bottom heater; 9—side thermocouple; 10—control thermocouple; 11—top heater; 12—tube heater.

Iron nanopowder and nitrogen were used as a source for  $\text{Fe}_2\text{N}$ . Ceramic crucible with initial powder was put into the tube furnace (BTF-1700C, (Hefei, China). The tube has been purged by ammonia ( $\text{NH}_3$ ) for 30 min before synthesis. Synthesis was carried out in  $\text{NH}_3$  atmosphere at  $530\text{ }^\circ\text{C}$  for 6 h with a heat rate of  $8\text{ }^\circ\text{C}/\text{min}$ . Mechanically mixed and powder was hot pressed for 2 h at  $1100\text{ }^\circ\text{C}$ . The received hot-pressed sample was heated in  $\text{N}_2$  atmosphere for 10 h at  $700\text{ }^\circ\text{C}$  (heat rate was  $5\text{ }^\circ\text{C}/\text{min}$ ). After heat treatment, the sample was mechanically ground into ivory-colored powder.

XRD analysis was held with a Bruker D8 Advance (Karlsruhe, Germany) with a step of  $0.02^\circ$ . Structural parameters were refined by the Rietveld method using TOPAS5 software.

X-ray diffraction analysis (XRD) was used as the structure analysis method for the synthesized nitrides powders investigated. XRD analysis was performed with a Bruker D8 ADVANCE diffractometer with a vertical goniometer and  $\text{Cu K}\alpha$ -radiation. The diffraction angles ( $2\theta$ ) are  $5\text{--}100^\circ$ ,  $10\text{--}80^\circ$ , and  $5\text{--}120^\circ$  for  $\text{Li}_3\text{N}$ ,  $\text{Fe}_2\text{N}$ , and  $\text{Li}_3\text{FeN}_2$ , respectively.

Calorimetric measurements were performed using a TAM IV Microcalorimeter (Shanghai, China) at 298 K with the cell volume of 20 mL. Aqueous solution of  $1\text{ mol dm}^{-3}$  HCl was used for the calorimetric cell ampoule. The ampoule was broken when thermal equilibrium was established, and nitride powder began to dissolve in HCl solution. Thermo-EMF vs. time was registered during the dissolution process providing the heat dissolution curve. Integration of this curve gave the value of dissolution enthalpy.

### 3. Results

Figure 2 shows the XRD pattern of synthesized  $\text{Li}_3\text{N}$  (a) and  $\text{Fe}_2\text{N}$  (b) powders. All peaks are in good correlation with database one.  $\text{Li}_3\text{N}$  has a  $P6/mmm$  space group with lattice parameters  $a = 3.6711\text{ \AA}$ ,  $b = 3.6711\text{ \AA}$ , and  $c = 3.8770\text{ \AA}$ , which are in good correlation with [74] and PDF #30-0759.  $\text{Fe}_2\text{N}$  reflection peaks also are in good correlation with [75]

and PDF #50-0978. The space group of  $\text{Fe}_2\text{N}$  is  $P312$  with lattice parameters  $a = 4.7912 \text{ \AA}$ ,  $b = 4.7912 \text{ \AA}$ , and  $c = 4.416 \text{ \AA}$ .

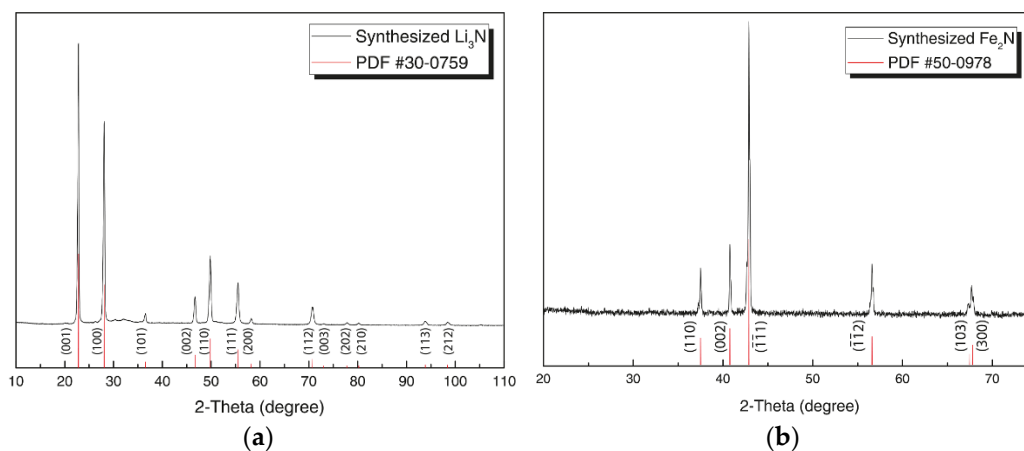


**Figure 2.** XRD pattern of synthesized (a)  $\text{Li}_3\text{N}$  at  $170 \text{ }^\circ\text{C}$  for 5 h at  $\text{N}_2$  atmosphere (709 kPa) and (b)  $\text{Fe}_2\text{N}$  at  $530 \text{ }^\circ\text{C}$  for 5 h at  $\text{NH}_3$  atmosphere.

Figure 3 shows the XRD pattern of  $\text{Li}_3\text{N}$ ,  $\text{Fe}_2\text{N}$ , and  $\text{Li}_3\text{FeN}_2$  after heat treatment in a Netzsch APTAK chamber, tube furnace with ammonia atmosphere, and tube furnace with nitrogen atmosphere, respectively. Lattice parameters,  $a$  and  $c$ , calculated by the Rietveld method for  $\text{Li}_3\text{FeN}_2$  are  $a = 4.872 \text{ \AA}$ ,  $b = 9.677 \text{ \AA}$ , and  $c = 4.792 \text{ \AA}$ , respectively, in the  $Ibam$  space group. XRD patterns of  $\text{Li}_3\text{FeN}_2$  synthesized at different temperatures are shown in Figure 3. The sample synthesized at  $850 \text{ }^\circ\text{C}$  shows a high purity of 97.2% with  $\text{Li}_2\text{O}$  impurity. Other samples include such impurities as  $\text{Li}_2\text{O}$  (PDF #01-076-9237),  $\text{Li}_5\text{FeO}_4$  (PDF #01-075-1253), and  $\text{LiFeO}_2$  (PDF #74-2284). Samples synthesized at  $850 \text{ }^\circ\text{C}$  have only  $\text{Li}_2\text{O}$  impurity; thus, further investigation of the compounds were conducted with materials synthesized at  $850 \text{ }^\circ\text{C}$ .

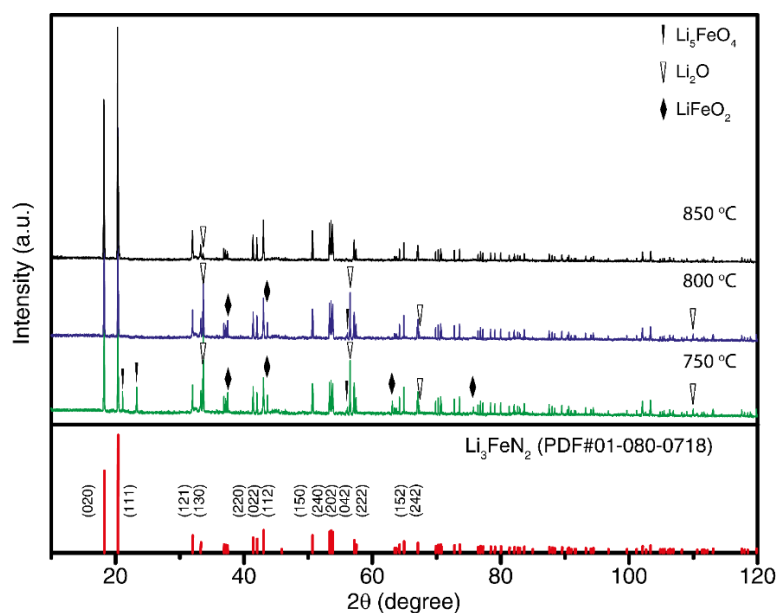


**Figure 3.** XRD patterns of  $\text{Li}_3\text{FeN}_2$  after heat treatment at 750, 800, and  $850 \text{ }^\circ\text{C}$  for 10 h in  $\text{N}_2$  atmosphere. The lines in the bottom indicate the diffraction positions of the  $\text{Li}_3\text{FeN}_2$  structure (PDF #01-080-0718).

The structure refinement defined that Li<sup>+</sup> is in 4b and 8g, Fe<sup>+3</sup> is in 4a, and N<sup>-3</sup> is in 8j sites. All calculations were carried out with using TOPAS 4 software by Bruker. The final structure parameters (including site occupancy) are listed in Table 2.

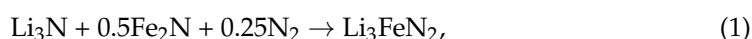
**Table 2.** Structure characteristics of Li<sub>3</sub>FeN<sub>2</sub>.

Atom/Void	Site	g	x	y	z
Li <sub>1</sub>	8g	0.91	0.0	0.25745	0.25
Li <sub>2</sub>	4b	1	0.0	0.5	0.25
Fe	4a	1	0.0	0.0	0.25
N	8j	0.98	0.219979	0.113757	0.5

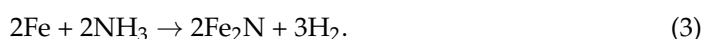
## 4. Discussion

### 4.1. The Standard Enthalpy of Formation

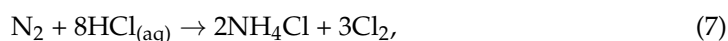
The formation enthalpy of Li<sub>3</sub>FeN<sub>2</sub> (LFN) compound from single nitrides Li<sub>3</sub>N and Fe<sub>2</sub>N is calculated using the following equation ( $\Delta_{\text{ox}}H_{\text{LFN}}$ ):



and single nitrides were synthesized by reactions, as described in the Experimental section:



For enthalpy calculation, we used thermodynamic cycle with the following reactions, as shown in Figure 4:



where (aq) means “aqueous”. The standard enthalpy ( $\Delta_{\text{d}}H_{\text{LFN}}$ ) has been determined in the calorimeter. The received value was equal to  $-1972.96 \pm 25 \text{ J g}^{-1}$ , as shown in Table 3.

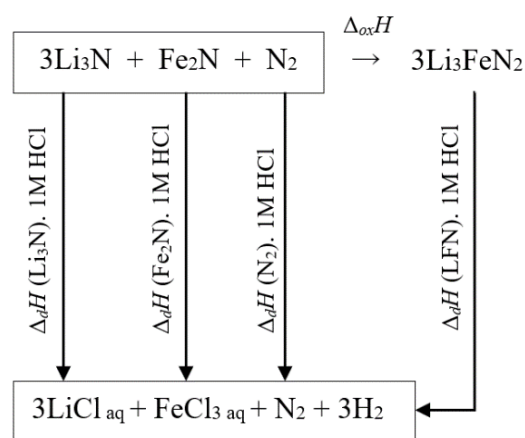


**Figure 4.** Thermochemical cycle scheme. Dissolution enthalpy connection of Li<sub>3</sub>FeN<sub>2</sub> with its formation enthalpies from single nitrides.

**Table 3.** Values of specific and molar enthalpies of dissolution (298 K, p = 101 kPa, 1 mol dm<sup>-3</sup> HCl).

Compound	Specific Enthalpy, J g <sup>-1</sup>	Molar Mass, g mol <sup>-1</sup>	Molar Enthalpy of Dissolution, kJ mol <sup>-1</sup>	Ref.
Li <sub>3</sub> N	-3163.853 ± 30	34.83	-110.197 ± 1.7	this work
Fe <sub>2</sub> N	-13.79 ± 1.5	125.701	-1.734 ± 0.04	this work
N <sub>2</sub>	-71.716 ± 10	28.014	-2.56 ± 0.12	this work
Li <sub>3</sub> FeN <sub>2</sub>	-1972.96 ± 25	104.684	-206.537 ± 2.8	this work
Li <sub>3</sub> Na <sub>3</sub> N <sub>2</sub>	-2285.96 ± 13.4	117.807	-269.3018	[66]

The resulting value of  $\Delta_{\text{ox}}H_{\text{LFN}}$  is obtained by the next equation:

$$\Delta_{\text{ox}}H_{\text{LFN}} = \Delta_{\text{d}}H_{\text{Li}_3\text{N}} + 0.5\Delta_{\text{d}}H_{\text{Fe}_2\text{N}} + 0.25\Delta_{\text{d}}H_{\text{N}_2} - \Delta_{\text{d}}H_{\text{LFN}}. \quad (8)$$

The values of  $\Delta_{\text{d}}H_{\text{Li}_3\text{N}}$ ,  $\Delta_{\text{d}}H_{\text{Fe}_2\text{N}}$ , and  $\Delta_{\text{d}}H_{\text{N}_2}$  were also measured by the calorimetry method. Measurement results are shown in Table 3. The value of  $\Delta_{\text{ox}}H_{\text{LFN}}$  by Equation (8) is equal to -94.833 kJ mol<sup>-1</sup>. The negative value of  $\Delta_{\text{ox}}H_{\text{LFN}}$  defines Li<sub>3</sub>FeN<sub>2</sub> as a stable phase. In addition, it is energetically favorable to synthesize LFN from single nitrides.

At last, the enthalpy of formation of Li<sub>3</sub>FeN<sub>2</sub> from elements can now be calculated using the following equation:

$$\Delta_{\text{f}}H_{\text{LFN}} = \Delta_{\text{f}}H_{\text{Li}_3\text{N}} + 0.5\Delta_{\text{f}}H_{\text{Fe}_2\text{N}} + 0.25\Delta_{\text{f}}H_{\text{N}_2} + \Delta_{\text{ox}}H_{\text{LFN}}. \quad (9)$$

Standard enthalpies for the calculation were taken from the handbooks [76,77], as shown in Table 4.

**Table 4.** Standard enthalpies of formation from elements ( $\Delta_{\text{f}}H^0$ ).

Compound	$\Delta_{\text{f}}H^0_{298-15}$ , kJ mol <sup>-1</sup>	Reference
Li <sub>3</sub> N <sub>(cryst)</sub>	-196.78 ± 0.3	[76]
Fe <sub>2</sub> N <sub>(cryst)</sub>	-3.77 ± 0.1	[76]
N <sub>2(gas)</sub>	8.67 ± 0.1	[77]
Li <sub>3</sub> FeN <sub>2(cryst)</sub>	-291.331 ± 5.7	this work
LiCaN <sub>(cryst)</sub>	-216.8 ± 10.8	[78]
Li <sub>3</sub> BN <sub>2(cryst)</sub>	-534.5 ± 16.7	[79]
Li <sub>3</sub> AlN <sub>2(cryst)</sub>	-567.8 ± 12.4	[79]
LiMoN <sub>2(cryst)</sub>	-386.0 ± 6.4	[80]
Li <sub>7</sub> MnN <sub>4</sub>	-661	[81]

The subscripts (cryst) and (gas) mean "crystalline" and "gaseous", correspondingly.

The calculated value of the enthalpy of Li<sub>3</sub>FeN<sub>2</sub> formation by Equation (9) is -291.331 ± 5.7 kJ mol<sup>-1</sup>, Table 4. The enthalpy of formation  $\Delta_{\text{f}}H^0$  for Li<sub>3</sub>FeN<sub>2</sub> has the same order as for similar compounds, namely lithium metal nitrides (Table 4). That fact indirectly confirms the correctness of measurements. The value of formation enthalpy, calculated by Equation (9), can be used in thermodynamic estimation and the modeling of Li<sub>3</sub>FeN<sub>2</sub> reactivity.

#### 4.2. The Isobaric Heat Capacity

The temperature dependence of the isobaric heat capacity of the Li<sub>3</sub>FeN<sub>2</sub> is shown in Figure 5. According to XRD data (Figure 3), the obtained powder material contains a certain amount of lithium oxide Li<sub>2</sub>O. This impurity quantity must be taken in consideration for valuation of the heat capacity of the Li<sub>3</sub>FeN<sub>2</sub>. This impurity could appear during the synthesis process or contact with oxygen in air atmosphere. XRD quantitative methods

have limitations, but the heat capacity of a two-phase system must be recalculated by additive consideration:

$$mC_p = m(\text{LFN})C_p(\text{LFN}) + m(\text{Li}_2\text{O})C_p(\text{Li}_2\text{O}), \quad (10)$$

where  $C_p$ —a specific heat capacity (pressure is constant), and  $m$ —a mass. The sample weight consists of synthesized compound ( $\text{Li}_3\text{FeN}_2$ ) and impurity ( $\text{Li}_2\text{O}$ ). So, the heat capacity of  $\text{Li}_3\text{FeN}_2$  is expressed from Equation (10) as:

$$C_p(\text{LFN}) = \frac{mC_p - m(\text{Li}_2\text{O})C_p(\text{Li}_2\text{O})}{m(\text{LFN})}. \quad (11)$$

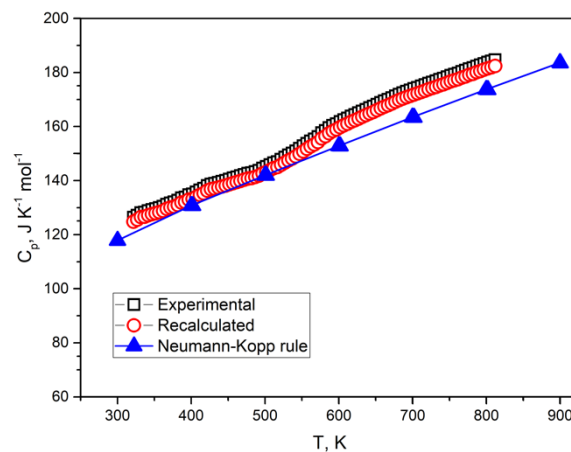


**Figure 5.** Temperature dependences of the experimental, recalculated, and Neumann–Kopp rule heat capacities of  $\text{Li}_3\text{FeN}_2$ . The line for the Neuman–Kopp rule is given as an approximating allometric line.

The weight of the included compounds can be found from the total mass of the sample, which are calculated through the weight fraction of lithium oxide,  $\omega(\text{Li}_2\text{O})$ :

$$m(\text{Li}_2\text{O}) = m\omega(\text{Li}_2\text{O}) \quad (12)$$

and

$$m(\text{LFN}) = m[1 - \omega(\text{Li}_2\text{O})]. \quad (13)$$

According to Equations (12) and (13), Equation (11) can be written as follows:

$$C_p(\text{LFN}) = \frac{C_p - C_p(\text{Li}_2\text{O})\omega(\text{Li}_2\text{O})}{1 - \omega(\text{Li}_2\text{O})}. \quad (14)$$

Thereby, the heat capacity of LFN can be calculated from the experimental data and heat capacity of lithium oxide impurity. For Equation (14), it is required to know the dependence of the specific heat capacity of the lithium oxide from temperature. For this, tabulated data for the lithium oxide heat capacity [77] were used. For the temperature range of 300–900 K, the commonly used polynomial formula for the heat capacity is as follows:

$$C_p = a + bT - cT^{-2} \quad (15)$$

where  $a$ ,  $b$ , and  $c$  are empirical coefficients;  $T$  is the absolute temperature. The received coefficients for lithium oxide are  $a = 76.666 \text{ J mol}^{-1} \text{ K}^{-1}$ ,  $b = -13.63 \cdot 10^{-3} \text{ J mol}^{-1} \text{ K}^{-2}$ , and  $c = -18.624 \cdot 10^5 \text{ J mol}^{-1} \text{ K}$ . The heat capacity of  $\text{Li}_3\text{FeN}_2$  for the 300–900 K temperature range was recalculated using Equations (15) and (16) considering  $\text{Li}_2\text{O}$ 's impurity presence. According to XRD data (Figure 3),  $\text{Li}_3\text{FeN}_2$  contains about  $2.8 \pm 0.04 \text{ wt } \% \text{ Li}_2\text{O}$ . The experimental and recalculated LFN heat capacity is shown in Figure 5 and Table 5. Empirical

values for heat capacity were calculated by the Neumann–Kopp rule. This rule prescribes calculating the molar heat capacity of a complex compound from the heat capacities of constituent elements by adding them in with the corresponding compound stoichiometry. However, this calculation method gives good results for room temperatures and rough results for high temperatures. For more accurate results, binary compounds were used instead of single elements:

$$C_p(\text{CN}) = \sum n(\text{BN})C_p(\text{BN}) \quad (16)$$

where  $C_p$ —molar heat capacity,  $n$ —a stoichiometric coefficient, and CN and BN are complex and binary nitrides, correspondingly. For LFN, Equation (16) can be written as (according to Equation (1)):

$$C_p(\text{LFN}) = C_p(\text{Li}_3\text{N}) + 0.5C_p(\text{Fe}_2\text{N}) + 0.25C_p(\text{N}_2). \quad (17)$$

**Table 5.** The temperature dependence of the experimental (exp.), recalculated by Equation (14) (rec.), and calculated by the Neumann–Kopp (N-K) rule (Equation (17)) heat capacities ( $C_p$ ) of  $\text{Li}_3\text{FeN}_2$ (s).

T, K	$C_p(\text{exp.}), \text{J K}^{-1} \text{mol}^{-1}$	$C_p(\text{rec.}), \text{J K}^{-1} \text{mol}^{-1}$	$C_p(\text{N-K}), \text{J K}^{-1} \text{mol}^{-1}$
300	126.9	124.1	117.8
400	134.1	132.6	130.7
500	146.3	144.3	141.9
600	160.5	158.3	152.8
700	173.8	171.9	163.4
800	183.3	180.7	173.6
900	186.1	178.8	183.5

The dependence of the heat capacity by temperature calculated from Equation (17) using tabular data [77] is shown in Figure 5 and Table 5.

The temperature dependence of the heat capacity calculated by the Neumann–Kopp rule is in good correlation with the recalculated heat capacity (considering  $\text{Li}_2\text{O}$  impurity amount). However, XRD quantitative analysis gives rough results for the small presence of compounds in the material. For other quantitative methods, the amount of impurities can be measured more accurately: for example, thermogravimetry or volumetric methods.

#### 4.3. Entropy

Entropy is another thermodynamic function that should be calculated. The Third Law of thermodynamics states, “The entropy of a perfect crystal is zero when the temperature of the crystal is equal to absolute zero (0 K)”. Thus, the entropy absolute value can be valued by the equation:

$$S(T) = \int_0^{T_1} \frac{C_p(T)}{T} dT + \frac{\Delta H_1}{T_1} + \int_{T_1}^{T_2} \frac{C_p(T)}{T} dT + \frac{\Delta H_2}{T_2} + \dots + \int_{T_k}^T \frac{C_p(T)}{T} dT \quad (18)$$

where  $S$  is entropy,  $\Delta H_k$  is enthalpy of the  $k$ -th phase transition, and  $T_k$  is temperature of the  $k$ -th phase transition ( $0 < T_k < T$ ). Since the entropy can be calculated by the Neumann–Kopp rule, if there is no phase transition until the calculation temperature, entropy can be also calculated by the Neumann–Kopp rule:

$$S(T) = \int_0^T \frac{\sum C_p(T, \text{BN})}{T} dT = \sum \int_0^T \frac{C_p(T, \text{BN})}{T} dT = \sum S(T, \text{BN}), \quad (19)$$



where BN is the binary nitride compound (see Equation (16)). According to Equations (16) and (17), Equation (19) can be written in the following way:

$$S(\text{LFN}) = S(\text{Li}_3\text{N}) + 0.5S(\text{Fe}_2\text{N}). \quad (20)$$

The entropy of  $\text{Li}_3\text{FeN}_2$  at room temperature is  $113.2 \text{ J mol}^{-1} \text{ K}^{-1}$  according to Equation (20) and tabular data [82]. The additive rule for entropy calculation is suitable if the sum of the molar volumes of binary compounds differs a bit from the molar volume of the complex compound [83]. Thus, the molar volume for  $\text{Li}_3\text{N}$  is  $27.2 \text{ cm}^3 \text{ mol}^{-1}$  ( $\rho = 1.28 \text{ g cm}^{-3}$  [83]), for  $\text{Fe}_2\text{N}$  is  $19.8 \text{ cm}^3 \text{ mol}^{-1}$  ( $\rho = 6.35 \text{ g cm}^{-3}$  [83]), and for  $\text{Li}_3\text{FeN}_2$  is  $33.9 \text{ cm}^3 \text{ mol}^{-1}$  ( $\rho = 3.09 \text{ g cm}^{-3}$  [84]). The sum of the molar volumes of binary nitrides with their corresponding coefficients is  $37.1 \text{ cm}^3 \text{ mol}^{-1}$  and differs about 9% from the LFN molar volume, which allows usage of an additive scheme.

In addition, the LFN entropy can be calculated by the W. Herz rule [85]:

$$S_{298}^0 = K_H (M/C_{p,298})^{1/3} m, \quad (21)$$

where  $K_H$  is Herz constant ( $K_H = 20.5$ ),  $M$  is molar mass,  $C_{p,298}$  is isobaric heat capacity, and  $m$  is atoms per formula. According to Equation (21) and considering  $C_{p,298}$  from Table 5, the LFN entropy is  $116.2 \text{ J mol}^{-1} \text{ K}^{-1}$ . Thus, the LFN entropy calculated by the Herz rule is in good correlation with the Neumann–Kopp rule result.

#### 4.4. The Standard Gibbs Free Energy

The enthalpy of formation and entropy calculated above allows evaluating the standard Gibbs free energy of  $\text{Li}_3\text{FeN}_2$  formation (at  $T = 298 \text{ K}$ ):

$$\Delta_f G_{298}^0 = \Delta_f H_{298}^0 - 298 \Delta_f S_{298}^0. \quad (22)$$

The resulting value of the Gibbs free energy for  $\text{Li}_3\text{FeN}_2$  at room temperature is  $-276.7 \text{ kJ mol}^{-1}$ .

The next reaction is suggested for the determination of stability against metallic lithium with subsequent calculation of the Gibbs free energy at room temperature:



To determine the Gibbs free energy of the reaction, it is required to subtract from  $\Delta_f G_{298}^0$  values of the Gibbs energy for initial reagents of the reaction. The  $\Delta_f G_{298}^0$  for single elements is equal to zero, and for  $\text{Li}_3\text{N}$ , it is  $-128.6 \text{ kJ mol}^{-1}$  [82]. The  $\text{Li}_3\text{FeN}_2$  Gibbs free energy has been calculated above. Thus, the Gibbs free energy for reaction (23) is  $19.5 \text{ kJ mol}^{-1}$ , and this reaction is thermodynamically impossible. Finally,  $\text{Li}_3\text{FeN}_2$  is stable against metallic lithium at room temperature.

## 5. Conclusions

The thermodynamic characteristics were determined for  $\text{Li}_3\text{FeN}_2$  anode material for a lithium-ion battery. The two-step synthesis method allowed producing a highly pure compound with less than 3 wt % of  $\text{Li}_2\text{O}$  impurity according to XRD data. The enthalpy of  $\text{Li}_3\text{FeN}_2$  formation from binary nitrides was determined according to the measured enthalpy of dissolution of reagents and product of  $\text{Li}_3\text{FeN}_2$  formation reaction. The obtained value is equal to  $-206.5 \pm 2.8 \text{ kJ mol}^{-1}$ . The  $\text{Li}_3\text{FeN}_2$  standard enthalpy of formation from single elements is equal to  $-291.3 \pm 5.7 \text{ kJ mol}^{-1}$ . This value can be used in further thermodynamic modeling and determinations.

The heat capacity value was recalculated considering the presence of  $\text{Li}_2\text{O}$  impurity. The temperature dependence of the heat capacity is in good correlation with calculation by the Neumann–Kopp rule. Finally, the heat capacity can be described by formula  $C_p(T) = 78.997 + 0.132 \times T + 4.654 \cdot 10^5 \times T^{-2}$ , where  $T$  is absolute temperature. The LFN

entropy is equal to  $113.2 \text{ J mol}^{-1} \text{ K}^{-1}$ , and the Gibbs free energy of  $\text{Li}_3\text{FeN}_2$  formation is  $-276.7 \text{ kJ mol}^{-1}$ . The calculations confirm that the  $\text{Li}_3\text{FeN}_2$  material is stable against metallic lithium. All thermodynamic values and functions can be used for modeling and further calculations.

**Author Contributions:** Conceptualization, A.P. and P.N.; methodology, D.A.; software, K.P.; validation, D.A., K.P. and Q.W.; formal analysis, A.P.; investigation, D.A. and K.P.; resources, Q.W.; data curation, P.N.; writing—original draft preparation, D.A.; writing—review and editing, P.N.; visualization, K.P.; supervision, A.P.; project administration, Q.W.; funding acquisition, Q.W. All authors have read and agreed to the published version of the manuscript.

**Funding:** The research is partially funded by the Ministry of Science and Higher Education of the Russian Federation: Advanced Digital Technologies (contract No. 075-15-2020-934 dated from 17 November 2020).

**Institutional Review Board Statement:** Not applicable.

**Informed Consent Statement:** Not applicable.

**Data Availability Statement:** The data presented in this study are available on request from the corresponding author.

**Conflicts of Interest:** The authors declare no conflict of interest.

## References

1. Bruce, P.G.; Scrosati, B.; Tarascon, J.M. Nanomaterials for rechargeable lithium batteries. *Angew. Chem. Int. Ed.* **2008**, *47*, 2930–2946. [[CrossRef](#)]
2. Du, F.H.; Li, S.Q.; Yan, Y.; Lu, X.M.; Guo, C.; Ji, Z.; Hu, P.; Shen, X. Facile fabrication of  $\text{Fe}_{0.8}\text{Mn}_{1.2}\text{O}_3$  with various nanostructures for high-performance lithium-ion batteries. *Chem. Eng. J.* **2022**, *427*, 131697. [[CrossRef](#)]
3. Faizan, M.; Hussain, S.; Vikraman, D.; Ali, B.; Kim, H.S.; Jung, J.; Nam, K.W.  $\text{MoS}_2@ \text{Mo}_2\text{C}$  hybrid nanostructures formation as an efficient anode material for lithium-ion batteries. *J. Mater. Res. Technol.* **2021**, *14*, 2382–2393. [[CrossRef](#)]
4. Yoon, J.; Choi, W.; Kim, H.; Choi, Y.S.; Kim, J.M.; Yoon, W.S. The effects of nanostructures on lithium storage behavior in  $\text{Mn}_2\text{O}_3$  anodes for next-generation lithium-ion batteries. *J. Power Sources* **2021**, *493*, 229682. [[CrossRef](#)]
5. Devi, V.S.; Athika, M.; Duraisamy, E.; Prasath, A.; Sharma, A.S.; Elumalai, P. Facile sol-gel derived nanostructured spinel  $\text{Co}_3\text{O}_4$  as electrode material for high-performance supercapattery and lithium-ion storage. *J. Energy Storage* **2019**, *25*, 100815. [[CrossRef](#)]
6. Kosova, N.V. Mechanochemical reactions and processing of nanostructured electrode materials for lithium-ion batteries. *Mater. Today Proc.* **2016**, *3*, 391–395. [[CrossRef](#)]
7. Duan, W.; Yan, W.; Yan, X.; Munakata, H.; Jin, Y.; Kanamura, K. Synthesis of nanostructured  $\text{Ni}_3\text{S}_2$  with different morphologies as negative electrode materials for lithium-ion batteries. *J. Power Sources* **2015**, *293*, 706–711. [[CrossRef](#)]
8. Wang, G.; Shen, X.; Yao, J. One-dimensional nanostructures as electrode materials for lithium-ion batteries with improved electrochemical performance. *J. Power Sources* **2009**, *189*, 543–546. [[CrossRef](#)]
9. Zhang, M.; Li, L.; Jian, X.; Zhang, S.; Shang, Y.; Xu, T.; Dai, S.; Xu, J.; Kong, D.; Wang, Y.; et al. Free-standing and flexible CNT/(Fe@Si@SiO<sub>2</sub>) composite anodes with kernel-pulp-skin nanostructure for high-performance lithium-ion batteries. *J. Alloys Compd.* **2021**, *878*, 160396. [[CrossRef](#)]
10. Liu, Y.; Sun, G.; Cai, X.; Yang, F.; Ma, C.; Xue, M.; Tao, X. Nanostructured strategies towards boosting organic lithium-ion batteries. *J. Energy Chem.* **2021**, *54*, 179–193. [[CrossRef](#)]
11. Nguyen, A.T.; Phung, V.D.; Mittova, V.O.; Ngo, H.D.; Vo, T.N.; Le Thi, M.L.; Mittova, I.Y.; Le, M.L.P.; Ahn, Y.N.; Kim, I.T.; et al. Fabricating nanostructured  $\text{HoFeO}_3$  perovskite for lithium-ion battery anodes via co-precipitation. *Scr. Mater.* **2022**, *207*, 114259. [[CrossRef](#)]
12. Lan, X.; Cui, J.; Yu, H.; Xiong, X.; Tan, L.; Hu, R. Nanostructured Sn–Mo multilayer film anode with stable electrode-interfaces for long-cycle lithium storage. *J. Power Sources* **2021**, *509*, 230391. [[CrossRef](#)]
13. Kakarla, A.K.; Narsimulu, D.; Yu, J.S. Two-dimensional porous  $\text{NiCo}_2\text{O}_4$  nanostructures for use as advanced high-performance anode material in lithium-ion batteries. *J. Alloys Compd.* **2021**, *886*, 161224. [[CrossRef](#)]
14. Woo, S.; Chung, K.; Bae, J.; Lee, Y.W.; Lee, S. Microwave-assisted hydrothermal synthesis of a high-voltage microcube  $\text{LiMn}_{1.5}\text{Ni}_{0.5}\text{O}_4$  spinel cathode material. *J. Electroanal. Chem.* **2021**, *902*, 115798. [[CrossRef](#)]
15. Kozawa, T.; Fukuyama, K.; Kondo, A.; Naito, M. Wet milling synthesis of  $\text{NH}_4\text{CoPO}_4 \cdot \text{H}_2\text{O}$  platelets: Formation reaction, growth mechanism, and conversion into high-voltage  $\text{LiCoPO}_4$  cathode for Li-ion batteries. *Mater. Res. Bull.* **2021**, *135*, 111149. [[CrossRef](#)]
16. Tolganbek, N.; Yerkinbekova, Y.; Kalybekkyzy, S.; Bakenov, Z.; Mentbayeva, A. Current state of high voltage olivine structured  $\text{LiMPO}_4$  cathode materials for energy storage applications: A review. *J. Alloys Compd.* **2021**, *882*, 160774. [[CrossRef](#)]
17. Hou, X.; Li, W.; Wang, Y.; Li, S.; Meng, Y.; Yu, H.; Chen, B.; Wu, X. Sodium-based dual-ion batteries via coupling high-capacity selenium/graphene anode with high-voltage graphite cathode. *Chin. Chem. Lett.* **2020**, *31*, 2314–2318. [[CrossRef](#)]

18. Pang, P.; Tan, X.; Wang, Z.; Cai, Z.; Nan, J.; Xing, Z.; Li, H. Crack-free single-crystal  $\text{LiNi}_{0.83}\text{Co}_{0.10}\text{Mn}_{0.07}\text{O}_2$  as cycling/thermal stable cathode materials for high-voltage lithium-ion batteries. *Electrochim. Acta* **2021**, *365*, 137380. [[CrossRef](#)]
19. Papp, J.K.; Li, N.; Kaufman, L.A.; Naylor, A.J.; Younesi, R.; Tong, W.; McCloskey, B.D. A comparison of high voltage outgassing of  $\text{LiCoO}_2$ ,  $\text{LiNiO}_2$ , and  $\text{Li}_2\text{MnO}_3$  layered Li-ion cathode materials. *Electrochim. Acta* **2021**, *368*, 137505. [[CrossRef](#)]
20. Peng, Q.; Wang, Y.; Yang, G. High crystallinity, preferred orientation and superior reversible capacity  $\text{P}_2\text{-Na}_{0.67}\text{Ni}_{0.25}\text{Mn}_{0.75}\text{O}_2$  thin film as cathode material for wide voltage sodium-ion battery. *Electrochim. Acta* **2020**, *337*, 135761. [[CrossRef](#)]
21. Zhang, X.; Zou, L.; Cui, Z.; Jia, H.; Engelhard, M.H.; Matthews, B.E.; Cao, X.; Xie, Q.; Wang, C.; Manthiram, A.; et al. Stabilizing ultrahigh-nickel layered oxide cathodes for high-voltage lithium metal batteries. *Mater. Today* **2021**, *44*, 15–24. [[CrossRef](#)]
22. Kasim, M.F.; Azizan, W.A.H.W.; Elong, K.A.; Kamarudin, N.; Yaakob, M.K.; Badar, N. Enhancing the structural stability and capacity retention of Ni-rich  $\text{LiNi}_{0.7}\text{Co}_{0.3}\text{O}_2$  cathode materials via Ti doping for rechargeable Li-ion batteries: Experimental and computational approaches. *J. Alloys Compd.* **2021**, *888*, 161559. [[CrossRef](#)]
23. Yang, M.; Hu, B.; Geng, F.; Li, C.; Lou, X.; Hu, B. Mitigating voltage decay in high-capacity  $\text{Li}_{1.2}\text{Ni}_{0.2}\text{Mn}_{0.6}\text{O}_2$  cathode material by surface  $\text{K}^+$  doping. *Electrochim. Acta* **2018**, *291*, 278–286. [[CrossRef](#)]
24. Kocak, T.; Wu, L.; Wang, J.; Savaci, U.; Turan, S.; Zhang, X. The effect of vanadium doping on the cycling performance of  $\text{LiNi}_{0.5}\text{Mn}_{1.5}\text{O}_4$  spinel cathode for high voltage lithium-ion batteries. *J. Electroanal. Chem.* **2021**, *881*, 114926. [[CrossRef](#)]
25. Xu, Y.S.; Zhou, Y.N.; Zhang, Q.H.; Qi, M.Y.; Guo, S.J.; Luo, J.M.; Sun, Y.G.; Gu, L.; Cao, A.M.; Wan, L.J. Layered oxides with solid-solution reaction for high voltage potassium-ion batteries cathode. *Chem. Eng. J.* **2021**, *412*, 128735. [[CrossRef](#)]
26. Meng, J.; Zhang, S.; Liu, X.; Zhong, S.; Zou, Z. Facile Synthesis of 3D Urchin-like  $\text{V}_6\text{O}_{13}$  Microflowers as Cathode Materials for High-Capacity and High-Rate Lithium-Ion Batteries. *J. Electroanal. Chem.* **2021**, *900*, 115742. [[CrossRef](#)]
27. Deng, W.; Shi, W.; Liu, Q.; Jiang, J.; Wang, Q.; Guo, C. Conductive nonconjugated radical polymer as high capacity organic cathode material for high-energy Li/Na ion batteries. *J. Power Sources* **2020**, *479*, 228796. [[CrossRef](#)]
28. Zhang, S.; Zou, Z.; Zhang, H.; Liu, J.; Zhong, S. Al/Ga co-doped  $\text{V}_6\text{O}_{13}$  nanorods with high discharge specific capacity as cathode materials for lithium-ion batteries. *J. Electroanal. Chem.* **2021**, *890*, 115220. [[CrossRef](#)]
29. Lin, J.; Chen, S.; Zhu, L.; Yuan, Z.; Liu, J. Soft-template fabrication of hierarchical nanoparticle iron fluoride as high-capacity cathode materials for Li-ion batteries. *Electrochim. Acta* **2020**, *364*, 137293. [[CrossRef](#)]
30. Wu, Z.L.; Xie, H.; Li, Y.; Zhang, F.; Wang, Z.; Zheng, W.; Yang, M.; Xu, Z.; Lu, Z.  $2\text{Ni}_{0.25}\text{Mn}_{0.55}\text{O}_2$ : A high-capacity cathode material with a homogeneous monoclinic  $\text{Li}_2\text{MnO}_3$ -like superstructure. *J. Alloys Compd.* **2020**, *827*, 154202. [[CrossRef](#)]
31. Park, J.S.; Cho, J.S.; Kim, J.H.; Choi, Y.J.; Kang, Y.C. Electrochemical properties of micron-sized  $\text{Co}_3\text{O}_4$  hollow powders consisting of size controlled hollow nanospheres. *J. Alloys Compd.* **2016**, *689*, 554–563. [[CrossRef](#)]
32. Lu, Y.; Yu, L.; Wu, M.; Wang, Y.; Lou, X.W. Construction of complex  $\text{Co}_3\text{O}_4@ \text{Co}_3\text{V}_2\text{O}_8$  hollow structures from metal–organic frameworks with enhanced lithium storage properties. *Adv. Mater.* **2018**, *30*, 1702875. [[CrossRef](#)] [[PubMed](#)]
33. Chen, Y.; Xiang, K.; Zhu, Y.; Xiao, L.; Chen, W.; Liao, H.; Chen, X.; Chen, H. Porous, nitrogen-doped  $\text{Li}_3\text{V}_2(\text{PO}_4)_3/\text{C}$  cathode materials derived from oroxylum and their exceptional electrochemical properties in lithium-ion batteries. *Ceram. Int.* **2019**, *45*, 4980–4989. [[CrossRef](#)]
34. Kim, N.Y.; Yim, T.; Lee, Z. A novel specimen preparation of porous cathode materials in lithium-ion batteries for high-resolution transmission electron microscopy. *Mater. Charact.* **2019**, *155*, 109804. [[CrossRef](#)]
35. Qiu, S.; Fang, T.; Zhu, Y.; Hua, J.; Chu, H.; Zou, Y.; Zeng, J.L.; Xu, F.; Sun, L.  $2\text{Mn}_{0.6}\text{Ni}_{0.2}\text{O}_2$  with 3D porous rod-like hierarchical micro/nanostructure for high-performance cathode material. *J. Alloys Compd.* **2019**, *790*, 863–870. [[CrossRef](#)]
36. Gajraj, V.; Azmi, R.; Darma, M.S.D.; Indris, S.; Ehrenberg, H.; Mariappan, C.R. Correlation between structural, electrical and electrochemical performance of Zn doped high voltage spinel  $\text{LiNi}_{0.5-x}\text{Zn}_x\text{Mn}_{1.5}\text{O}_4$  porous microspheres as a cathode material for Li-Ion batteries. *Ceram. Int.* **2021**, *47*, 35275–35286. [[CrossRef](#)]
37. Zhang, H.; Li, J.; Luo, L.; Zhao, J.; He, J.; Zhao, X.; Liu, H.; Qin, Y.; Wang, F.; Song, J. Hierarchically porous MXene decorated carbon coated  $\text{LiFePO}_4$  as cathode material for high-performance lithium-ion batteries. *J. Alloys Compd.* **2021**, *876*, 160210. [[CrossRef](#)]
38. Zhou, Z.; Luo, Z.; He, Z.; Zheng, J.; Li, Y. A novel hollow porous structure designed for  $\text{Na}_{0.44}\text{Mn}_{2/3}\text{Co}_{1/6}\text{Ni}_{1/6}\text{O}_2$  cathode material of sodium-ion batteries. *J. Power Sources* **2020**, *479*, 228788. [[CrossRef](#)]
39. Li, Y.; Jiang, W.; Ding, G.; Yan, F.; Jing, X.; Zhu, Z.; Gao, Y.; Wu, L.; Xu, G.; Sun, F. Hierarchically porous  $\text{LiMn}_{0.1}\text{Fe}_{0.9}\text{PO}_4@ \text{C}$  microspherical cathode materials prepared by a facile template-free hydrothermal method for high-performance lithium-ion batteries. *J. Alloys Compd.* **2021**, *859*, 157825. [[CrossRef](#)]
40. Karami, M.; Masoudpanah, S.M.; Rezaie, H.R. Solution combustion synthesis of hierarchical porous  $\text{LiFePO}_4$  powders as cathode materials for lithium-ion batteries. *Adv. Powder Technol.* **2021**, *32*, 1935–1942. [[CrossRef](#)]
41. Gu, H.; Wang, J.; Wang, Z.; Tong, J.; Qi, N.; Han, G.; Zhang, M. Self-assembled porous  $\text{LiNi}_{0.8}\text{Co}_{0.1}\text{Mn}_{0.1}\text{O}_2$  cathode materials with micro/nano-layered hollow morphologies for high-power lithium-ion batteries. *Appl. Surf. Sci.* **2021**, *539*, 148034. [[CrossRef](#)]
42. Zhang, Y.; Zhang, W.; Shen, S.; Yan, X.; Wu, A.; Yin, J.; Zhang, J. Hollow porous bowl-shaped lithium-rich cathode material for lithium-ion batteries with exceptional rate capability and stability. *J. Power Sources* **2018**, *380*, 164–173. [[CrossRef](#)]
43. Zhang, X.; Hou, M.; Tamirate, A.G.; Zhu, H.; Wang, C.; Xia, Y. Carbon coated nano-sized  $\text{LiMn}_{0.8}\text{Fe}_{0.2}\text{PO}_4$  porous microsphere cathode material for Li-ion batteries. *J. Power Sources* **2020**, *448*, 227438. [[CrossRef](#)]
44. Deng, B.; Chen, Y.; Wu, P.; Han, J.; Li, Y.; Zheng, H.; Xie, Q.; Wang, L.; Peng, D.L. Lithium-rich layered oxide nanowires bearing porous structures and spinel domains as cathode materials for lithium-ion batteries. *J. Power Sources* **2019**, *418*, 122–129. [[CrossRef](#)]

45. Balakrishnan, P.G.; Ramesh, R.; Kumar, T.P. Safety mechanisms in lithium-ion batteries. *J. Power Sources* **2006**, *155*, 401–414. [[CrossRef](#)]
46. Huang, W.; Feng, X.; Han, X.; Zhang, W.; Jiang, F. Questions and Answers Relating to Lithium-Ion Battery Safety Issues. *Cell Rep. Phys. Sci.* **2021**, *2*, 100285. [[CrossRef](#)]
47. Zhang, L.; Li, X.; Yang, M.; Chen, W. High-safety separators for lithium-ion batteries and sodium-ion batteries: Advances and perspective. *Energy Storage Mater.* **2021**, *41*, 522–545. [[CrossRef](#)]
48. Hu, G.; Huang, P.; Bai, Z.; Wang, Q.; Qi, K. Comprehensively analysis the failure evolution and safety evaluation of automotive lithium ion battery. *eTransportation* **2021**, *10*, 100140. [[CrossRef](#)]
49. Zhou, M.; Hu, L.; Chen, S.; Zhao, X. Different mechanical-electrochemical coupled failure mechanism and safety evaluation of lithium-ion pouch cells under dynamic and quasi-static mechanical abuse. *J. Power Sources* **2021**, *497*, 229897. [[CrossRef](#)]
50. Lyu, P.; Liu, X.; Qu, J.; Zhao, J.; Huo, Y.; Qu, Z.; Rao, Z. Recent advances of thermal safety of lithium ion battery for energy storage. *Energy Storage Mater.* **2020**, *31*, 195–220. [[CrossRef](#)]
51. Liang, L.; Yuan, W.; Chen, X.; Liao, H. Flexible, nonflammable, highly conductive and high-safety double cross-linked poly (ionic liquid) as quasi-solid electrolyte for high performance lithium-ion batteries. *Chem. Eng. J.* **2021**, *421*, 130000. [[CrossRef](#)]
52. Liu, Y.; Xia, Y.; Zhou, Q. Effect of low-temperature aging on the safety performance of lithium-ion pouch cells under mechanical abuse condition: A comprehensive experimental investigation. *Energy Storage Mater.* **2021**, *40*, 268–281. [[CrossRef](#)]
53. Aikhuele, D.O. Development of a fixable model for the reliability and safety evaluation of the components of a commercial lithium-ion battery. *J. Energy Storage* **2020**, *32*, 101819. [[CrossRef](#)]
54. Mo, L.; Zheng, H. Solid coated  $\text{Li}_4\text{Ti}_5\text{O}_{12}$  (LTO) using polyaniline (PANI) as anode materials for improving thermal safety for lithium ion battery. *Energy Rep.* **2020**, *6*, 2913–2918. [[CrossRef](#)]
55. Münster, P.; Diehl, M.; Frerichs, J.E.; Börner, M.; Hansen, M.R.; Winter, M.; Niehoff, P. Effect of Li plating during formation of lithium ion batteries on their cycling performance and thermal safety. *J. Power Sources* **2021**, *484*, 229306. [[CrossRef](#)]
56. Yiding, L.; Wenwei, W.; Cheng, L.; Xiaoguang, Y.; Fenghao, Z. A safety performance estimation model of lithium-ion batteries for electric vehicles under dynamic compression. *Energy* **2021**, *215*, 119050. [[CrossRef](#)]
57. Yan, H.; Zhang, D.; Duo, X.; Sheng, X. A review of spinel lithium titanate ( $\text{Li}_4\text{Ti}_5\text{O}_{12}$ ) as electrode material for advanced energy storage devices. *Ceram. Int.* **2021**, *47*, 5870–5895. [[CrossRef](#)]
58. Ferg, E.; Gummow, R.D.; De Kock, A.; Thackeray, M.M. Spinel anodes for lithium-ion batteries. *J. Electrochem. Soc.* **1994**, *141*, L147. [[CrossRef](#)]
59. Jin, Y.; Zhu, B.; Lu, Z.; Liu, N.; Zhu, J. Challenges and recent progress in the development of Si anodes for lithium-ion battery. *Adv. Energy Mater.* **2017**, *7*, 1700715. [[CrossRef](#)]
60. Wilkening, M.; Amade, R.; Iwaniak, W.; Heitjans, P. Ultraslow Li diffusion in spinel-type structured  $\text{Li}_4\text{Ti}_5\text{O}_{12}$ —A comparison of results from solid state NMR and impedance spectroscopy. *Phys. Chem. Chem. Phys.* **2007**, *9*, 1239–1246. [[CrossRef](#)]
61. Yuan, T.; Tan, Z.; Ma, C.; Yang, J.; Ma, Z.F.; Zheng, S. Challenges of spinel  $\text{Li}_4\text{Ti}_5\text{O}_{12}$  for lithium-ion battery industrial applications. *Adv. Energy Mater.* **2017**, *7*, 1601625. [[CrossRef](#)]
62. Aravindan, V.; Lee, Y.S.; Madhavi, S. Research progress on negative electrodes for practical Li-ion batteries: Beyond carbonaceous anodes. *Adv. Energy Mater.* **2015**, *5*, 1402225. [[CrossRef](#)]
63. Nitta, N.; Wu, F.; Lee, J.T.; Yushin, G. Li-ion battery materials: Present and future. *Mater. Today* **2015**, *18*, 252–264. [[CrossRef](#)]
64. Schön, J.C.; Wevers, M.A.C.; Jansen, M. Investigation of the possible ternary nitrides in the system  $\text{Li}_3\text{N}/\text{Na}_3\text{N}$ . *Solid State Sci.* **2000**, *2*, 449–456. [[CrossRef](#)]
65. Somer, M.; Carrillo-Cabrera, W.; Peters, E.M.; Peters, K.; Von Schnering, H.G. Crystal structure of lithium beryllium nitride,  $\text{LiBeN}$ . *Z. Krist.-Cryst. Mater.* **1996**, *211*, 635. [[CrossRef](#)]
66. Yamane, H.; Okabe, T.H.; Ishiyama, O.; Waseda, Y.; Shimada, M. Ternary nitrides prepared in the  $\text{Li}_3\text{N}-\text{Mg}_3\text{N}_2$  system at 900–1000 K. *J. Alloys Compd.* **2001**, *319*, 124–130. [[CrossRef](#)]
67. Nishijima, M.; Takeda, Y.; Imanishi, N.; Yamamoto, O.; Takano, M. Li deintercalation and structural change in the lithium transition metal nitride  $\text{Li}_3\text{FeN}_2$ . *J. Solid State Chem.* **1994**, *113*, 205–210. [[CrossRef](#)]
68. Emery, N.; Sougrati, M.T.; Panabièrre, E.; Bach, S.; Fraisse, B.; Jumas, J.C.; Pereira-Ramos, J.P.; Willmann, P. Unidimensional unit cell variation and  $\text{Fe}^{+3}/\text{Fe}^{+4}$  redox activity of  $\text{Li}_3\text{FeN}_2$  in Li-ion batteries. *J. Alloys Compd.* **2017**, *696*, 971–979. [[CrossRef](#)]
69. Panabièrre, E.; Emery, N.; Lorthioir, C.; Sougrati, M.T.; Jumas, J.C.; Bach, S.; Pereira-Ramos, J.P.; Smith, R.I.; Willmann, P. Structural reinvestigation of  $\text{Li}_3\text{FeN}_2$ : Evidence of cationic disorder through XRD, solid-state NMR and Mössbauer spectroscopy. *J. Phys. Chem. Solids* **2016**, *95*, 37–42. [[CrossRef](#)]
70. Frankenburger, W.; Andrussow, L.; Dürr, F. Eine neue Komplexverbindung von Lithium, Eisen und Stickstoff. Ein Beitrag zur Frage der Stickstoffbindung an Eisen. *Z. Elektrochem. Angew. Phys. Chem.* **1928**, *34*, 632–637.
71. Fromont, M. Preparation and Study of Double Nitride  $\text{Li}_3\text{FeN}_2$ . *Rev. Chim. Miner.* **1967**, *4*, 447.
72. Langmi, H.W.; Culligan, S.D.; McGrady, G.S. Mixed-metal  $\text{Li}_3\text{N}$ -based systems for hydrogen storage:  $\text{Li}_3\text{AlN}_2$  and  $\text{Li}_3\text{FeN}_2$ . *Int. J. Hydrogen Energy* **2009**, *34*, 8108–8114. [[CrossRef](#)]
73. Wang, P.; Guo, J.; Xiong, Z.; Wu, G.; Wang, J.; Chen, P. The interactions of  $\text{Li}_3\text{FeN}_2$  with  $\text{H}_2$  and  $\text{NH}_3$ . *Int. J. Hydrogen Energy* **2016**, *41*, 14171–14177. [[CrossRef](#)]
74. Cabana, J.; Ling, C.D.; Oró-Solé, J.; Gautier, D.; Tobias, G.; Adams, S.; Canadell, E.; Palacin, M.R. Antifluorite-type lithium chromium oxide nitrides: Synthesis, structure, order, and electrochemical properties. *Inorg. Chem.* **2004**, *43*, 7050–7060. [[CrossRef](#)]

75. Lei, X.; Wang, J.; Peng, R.; Wang, W. The controllable magnetic properties of Fe<sub>3</sub>N nanoparticles synthesized by a simple urea route. *Mater. Res. Bull.* **2020**, *122*, 110662. [[CrossRef](#)]
76. Veryatin Ud Mashirev, V.P.; Ryabtsev, N.G.; Tarasov, V.I.; Rogozkin, B.D.; Korobov, I.V. *Termodinamicheskie Svoitsva Neorganicheskikh Veshchestv*; Atomizdat: Moscow, Russia, 1965.
77. Glushko, V.P.; Gurvich, L.V.; Bergman, G.A.; Veits, I.V.; Medvedev, V.A.; Khachkuruzov, G.A.; Yungman, V.S. *Termodinamicheskie Svoitsva Individual'nykh Veshchestv*; Nauka: Moscow, Russia, 1978.
78. McHale, J.M.; Navrotsky, A.; Kowach, G.R.; Balbarin, V.E.; DiSalvo, F.J. Energetics of Ternary Nitrides: Li–Ca–Zn–N and Ca–Ta–N Systems. *Chem. Mater.* **1997**, *9*, 1538–1546. [[CrossRef](#)]
79. McHale, J.M.; Navrotsky, A.; DiSalvo, F.J. Energetics of Ternary Nitride Formation in the (Li, Ca)–(B, Al)–N System. *Chem. Mater.* **1999**, *11*, 1148–1152. [[CrossRef](#)]
80. Elder, S.H.; DiSalvo, F.J.; Topor, L.; Navrotsky, A. Thermodynamics of ternary nitride formation by ammonolysis: Application to lithium molybdenum nitride (LiMoN<sub>2</sub>), sodium tungsten nitride (Na<sub>3</sub>WN<sub>3</sub>), and sodium tungsten oxide nitride (Na<sub>3</sub>WO<sub>3</sub>N). *Chem. Mater.* **1993**, *5*, 1545–1553. [[CrossRef](#)]
81. He, G.; Herbst, J.F.; Ramesh, T.N.; Pinkerton, F.E.; Meyer, M.S.; Nazar, L. Investigation of hydrogen absorption in Li<sub>7</sub>VN<sub>4</sub> and Li<sub>7</sub>MnN<sub>4</sub>. *Phys. Chem. Chem. Phys.* **2011**, *13*, 8889–8893. [[CrossRef](#)]
82. Pankratz, L.B. *Thermodynamic Properties of Carbides, Nitrides, and Other Selected Substances*; U.S. Department of the Interior: Washington, DC, USA, 1995.
83. Knunyants, I.L. *Khimicheskaya Entsiklopediya*; Sovetskaya Entsiklopediya: Moscow, Russia, 1988.
84. Gudat, A.; Kniep, R.; Rabenau, A.; Bronger, W.; Ruschewitz, U. Li<sub>3</sub>FeN<sub>2</sub>, a ternary nitride with <sup>1</sup>∞[FeN<sub>4</sub>23–] chains: Crystal structure and magnetic properties. *J. Less Common Met.* **1990**, *161*, 31–36. [[CrossRef](#)]
85. Morachevskiy, A.G.; Sladkov, I.B.; Firsova Ye, G. *Termodinamicheskiye Raschety v Khimii i Metallurgii*; Lan': St. Petersburg, Russia, 2018.